Mathematical Modeling and Algorithm Application
ISSN: 3006-0842 | Vol. 8, No. 1, 2026

Shock Plasticity and Spallation Behavior of Nanoporous Nickel

Hu Xiang[1,*], Yi Liao[1], Yihan Li[1], Tao Wen[2]

[1]School of Mechanical Engineering, Southwest Petroleum University, Chengdu, 610500, China

[2]Well Testing Company, Western Drilling Engineering Company Limited, China National Petroleum Corporation, Karamay City, 834000, China

[*] **Corresponding author**: Hu Xiang (Email: 3118520595@qq.com)

Abstract: This study employs large-scale molecular dynamics simulations to investigate the dynamic response of nanoporous nickel under impact loading, focusing on the influence of porosity and void distribution on stress, velocity, temperature, and density evolution over time, as well as on spalling strength. Results indicate that the presence of voids significantly weakens the impact strength of nanoporous nickel, with greater porosity leading to more pronounced weakening effects. Differences in void distribution affect the propagation characteristics of shock waves within the material. The study further discovered that both void collapse and spalltion induce localized high temperatures. Under identical impact conditions, spalling strength decreases with increasing porosity; even at the same porosity, varying void distributions cause fluctuations in spalling strength. Furthermore, this study revealed two synergistic mechanisms of void collapse—forward flow and lateral flow—and analyzed atomic displacement characteristics between voids under varying impact intensities: At lower impact intensities, atoms primarily fill adjacent voids bilaterally; at higher impact intensities, atoms migrate along the impact direction and participate in the collapse process.

Keywords: Nickel; Shock loading; Spallation; Nano-porous materials.

1. Introduction

Metal nanoporous materials represent a rapidly developing class of porous materials in recent years, finding extensive applications across multiple fields including catalytic sensors, energy storage, and blast protection. When shock waves propagate through nanoporous materials, energy associated with impact and explosive loads can be attenuated and dissipated. Due to their unique properties, they are extensively employed in various engineering applications, such as designing blast-resistant safety shells for high-speed railway tunnels and noise-reducing porous structures[1,2]。For these applications, understanding the thermomechanical behavior of metallic nanoporous materials under impact loading is crucial[3]。

Over the years, extensive research (theoretical, experimental, simulation, etc.) has been conducted to investigate shock wave damping, energy absorption characteristics, and impact damage in porous metals (e.g., gold, copper, aluminum, silver). Due to rapid pore growth and collapse, micro-acceleration fields form around pore boundaries. These localized acceleration forces, termed micro-inertial effects, play a crucial role in pore volume changes[4]。In quasi-static experiments, Bonnan et al.[5] observed the influence of coupling between pore collapse and plastic deformation on the matrix. Numerically, Erhart et al.[6] demonstrated that pore-pore interactions and collective effects significantly impact plastic deformation, with individual pores acting as dislocation sources whose efficiency is further enhanced through concentrated action. Krasnikov et al.[7] observed that reducing the ratio of pore radius to system size increases tensile strength, while elevated temperatures cause nearly linear decreases in tensile strength. To predict shock wave propagation and attenuation within materials, deriving the Hugoniot relations for these materials is also essential.

The primary applications of porous materials involve impact and explosion scenarios, making their shock response a subject of extensive research. Due to the diversity of materials and pore structures, challenges in studying nanomaterials primarily center on modeling and validation. Consequently, several researchers have developed models for stress wave propagation in ideal porous media[8-13].Most notably, Polenov and Chigarev[13] developed a closed system of constitutive equations for the dynamics and geometry of fluid-saturated heterogeneous elastic porous media within the framework of three-dimensional elasticity theory. Utilizing Fermi's principle, they derived the geometric characteristics of wavefronts and rays in fluid-saturated heterogeneous media.

Nanoporous nickel can be prepared via electrochemical dealloying[14]。Current research indicates that the mechanical properties of nanoporous metallic materials correlate with temperature, porosity, pore spacing, and the connectivity and length of ligaments[15,16]。These studies primarily analyze the microdeformation mechanisms and constitutive models of porous materials from the perspectives of pore nucleation, growth, and coalescence[7,17-20]。

This paper systematically investigates the impact response of nano-uniform-porous Ni and nano-gradient-porous Ni. It focuses on the effects of porosity and pore distribution on stress, velocity, temperature, and density wave profiles, as well as spalling strength in nano-porous Ni materials. Additionally, it addresses several issues previously explored in depth through molecular dynamics simulations, including pore collapse mechanisms and delamination fracture.

2. Methods and Modeling

The atomic interaction potential for Ni used in this study is described by the Exact Embedded Atomic Method (EAM) potential developed by Zhou et al.[21].Prior to investigating the impact response of nanoporous Ni, the EAM potential function is validated by comparing Hugoniot curves with simulation results presented below. The Hugoniot curves are computed using the multiscale method proposed by Reed et al.[22]. Molecular dynamics simulations are performed using the open-source software LAMMPS, and atomic structures are analyzed with the visualization software OVITO.

The complete Ni sample (sc-Ni) consists of 300 × 60 × 60 unit cells, containing 4,320,000 atoms. The np-Ni sample with a gradient void radius was obtained by removing atoms from five spherical voids in the sc-Ni sample. The nickel lattice constant is a = 3.52 Å. The x, y, and z axes align with the [100], [010], and [001] crystal directions, respectively. Energy minimization was first performed on sc-Ni using the conjugate gradient method. Subsequently, the sc-Ni sample was relaxed for 40 ps in the NPT ensemble at 0 GPa and 300 K to reach equilibrium. The time step for relaxation and equilibrium processes was set to 0.0002 ps. Fig. 1(a) shows the external structure of the simulation model, while Fig. 1(b) illustrates the distribution of the gradient-porosity sample with five voids. Two gradient-porosity samples with distinct porosities were employed: 3.73% and 10.91%. Following pore generation, each sample underwent energy minimization and NPT equilibrium at 300 K and 0 GPa. A relaxation time exceeding 40 ps was ensured for each sample to achieve complete equilibrium. Finally, Ni flyer impacted the specimens along the x-direction at velocities v = 0.5, 1.0, and 2.0 km/s, with the Ni specimen's initial velocity set to zero. The molecular dynamics simulation employed a time step of 0.0002 ps to ensure numerical stability, with the impact simulation duration set to 80 ps. To eliminate edge effects in the shock wave, periodic boundary conditions were applied along the y and z directions, while free boundary conditions were applied along the x (Shock wave) direction (loading direction). For comparison, simulations were also performed on samples with uniform voids (Fig. 1(c)), ensuring consistent porosity between the uniform-void and gradient-void specimens. All geometric parameters of the simulated samples are listed in Table 1.

Table 1 All geometric dimensions of the model

Case	v	Porosity	Graded Void Sample Parameters								Uniform Void Sample Parameters		
			S	l	Gra	V1	V2	V3	V4	V5	Ru	Su	l
1	0.5	3.73%	55a	20a	3a	5a	8a	11a	14a	17a	12.4a	48a	20a
	1.0	3.73%	55a	20a	3a	5a	8a	11a	14a	17a	12.4a	48a	20a
	2.0	3.73%	55a	20a	3a	5a	8a	11a	14a	17a	12.4a	48a	20a
2	0.5	10.91%	35a	20a	5a	5a	10a	15a	20a	25a	17.8a	21a	20a
	1.0	10.91%	35a	20a	5a	5a	10a	15a	20a	25a	17.8a	21a	20a
	2.0	10.91%	35a	20a	5a	5a	10a	15a	20a	25a	17.8a	21a	20a

Among them:

A: Lattice constant of nickel, a = 3.52 Å; Vi (i = 1,2,3,4,5): Radius of five voids in the sample;

v: Impact velocity;

S: Distance between the end of the graded cavity specimen and the adjacent cavity wall (Fig. 1(b));

l: Distance between adjacent voids (Fig. 1(b) and (c));

Ru: Radius of five voids in the uniformly cavitated sample;

Su: Distance between the end of the uniformly cavitated sample and the adjacent cavity wall (Fig. 1(c));

Gra: Gradient of void radius.

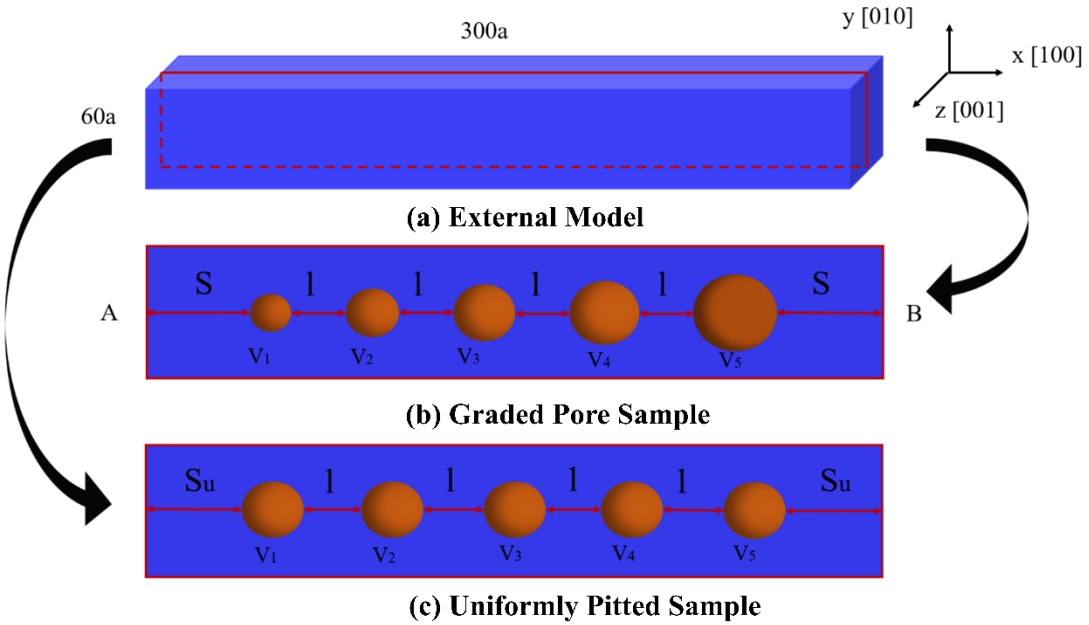


Figure 1. Simulation Model (a) External structure of the simulation model; (b) Hierarchical pore sample; (c) Uniform pore sample.

In this simulation, the molecular dynamics method was employed to model the impact process. The shock wave is

generated by a nickel metal impacting the target along the [100] direction. The simulation considers two loading directions for each gradient cavity target: G12345 and G54321. G12345 denotes the impact direction from A to B (Fig. 1(a)), while G54321 indicates the impact direction from B to A. Three model specimens (G12345, G54321, Uniform) were tested for each impact velocity. For analytical convenience, each specimen was labeled as Casei_G12345, Casei_G54321, and Casei_Uniform. To determine the position of each cavity, voids along the impact direction were sequentially labeled as V1, V2, V3, V4, and V5.

Through the following equation:

$$\left(E_d\right)_j^t = \left(\sum_{\alpha=1}^{N_j} E_{\alpha k}^t\right) - \left(E_{mk}\right)_j^t - \left(E_T^{initial}\right)_j^t \tag{1}$$

Where Ed is the kinetic energy of each atom α, and is the initial thermal energy prior to impact loading.

The virial stress of the atomic system is defined as：

$$\sigma = \frac{1}{\Omega}\left(-\sum_i m_i \bar{v}_i \cdot \bar{v}_i + \sum_i \sum_{j \neq i} \frac{1}{2}(x_j - x_i) \otimes f_{ij}\right) \tag{2}$$

Here, $m_i$represents the volume of the system, $\bar{v}_i$denotes the mass and thermal vibration velocity of atom i, and x_i indicates the position of atom i. f_{ij}signifies the interaction between atoms i and j. Within the stress components, positive stress indicates a compressive state, while negative stress indicates a tensile state.

Temperature calculations follow the law of energy distribution, namely：

$$T = \frac{1}{3Nk_B}\sum_{i=1}^{N} m_i\left(v_{ix}^2 + v_{iy}^2 + v_{iz}^2\right) \tag{3}$$

Here, K_b is the Boltzmann constant, m_i is the atomic mass of atom i, and v_{ix}^2, v_{iy}^2, v_{iz}^2 are the particle velocity components along the coordinate axes. For impact loads along the x-direction, the temperature is calculated by appropriately subtracting the velocity of each local center of mass along the impact direction. To minimize any errors associated with center-of-mass velocities, the temperature formula can be modified to exclude velocities in the impact direction without loss of accuracy, as shown below:

$$T = \frac{1}{3Nk_B}\sum_{i=1}^{N} m_i\left(v_{ix}^2 + v_{iy}^2 + v_{iz}^2\right) \tag{4}$$

Additionally, other physical quantities (such as temperature, density, and pressure) will be analyzed as functions of time and coordinates through binning analysis [23].

3. Results and discussion

3.1. Hugoniot Verification

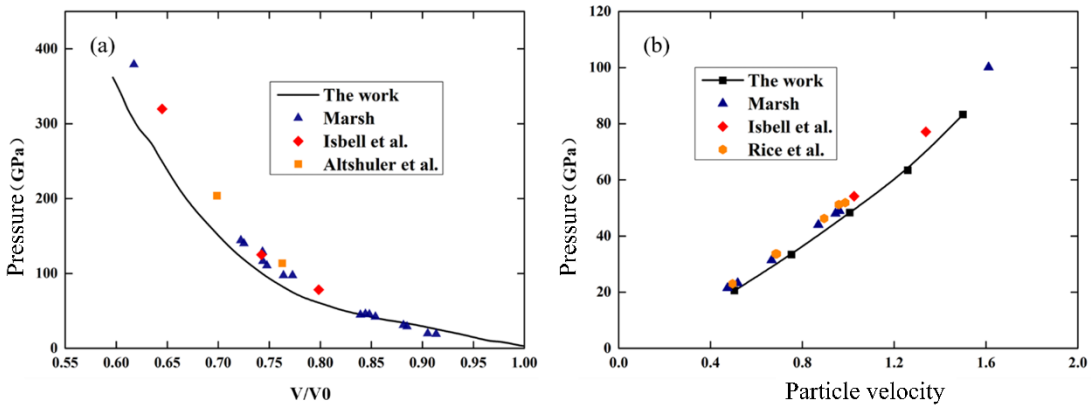


Figure 2. (a) Relationship between Hugoniot pressure (P) and specific volume (V/V₀); (b) Relationship between Hugoniot pressure (P) and particle velocity

The Hugoniot P-V/V₀ curve for metallic Ni is shown in Fig. 2(a), where P is pressure, V₀ is the initial volume, and V is the volume under compression. To validate the selected EAM potential under strong shock conditions, these curves are compared with experimental results reported by Marsh[24], Altshuler et al.[25], Isbell et al.[26] and Rice et al.[27].In Fig. 2(a), the solid line represents the curve calculated using the EAM potential in this work. The figure indicates that molecular dynamics simulations and experimental fits agree well when the compression ratio V/V₀ > 0.7; however, when V/V₀ < 0.7, the molecular dynamics-calculated pressure is significantly lower than the experimentally measured pressure. Therefore, in the simulations, the impact intensity was constrained to ensure V/V₀ > 0.7, with the corresponding pressure limit set at P < 150 GPa. Additionally, Fig. 2(b) compares the Hugoniot pressure-particle velocity relationship determined via molecular dynamics simulations in this work with experimental results, revealing that the simulated results closely resemble the experimental data.

3.2. Free-surface velocity curve and layer fracture strength

Experiments have demonstrated that the presence of pores during material compaction facilitates stress wave absorption, thereby reducing stress intensity. Layer fracture strength, as a key physical parameter reflecting a material's resistance to impact failure, can characterize the evolution of stress propagation in porous materials influenced by voids. Layer fracture strength (σ_{sp}) is defined as the maximum tensile stress during the fracture process. The stress time history curve is obtained using the binning method, and the maximum stress value at the moment of layer fracture is identified.

The free surface velocity evolution curves for Case 1 and Case 2 under different void distributions are plotted at v = 2.0 km/s, as shown in Fig. 3. The figure reveals that the free surface evolution curves for all models exhibit a similar trend: a sudden jump from zero to the maximum peak, followed by

decay to the first trough, and finally sustained oscillation. With identical impact intensity, the corresponding transition times at the same porosity are nearly identical: 19.6 ps and 20.1 ps for Fig.s 3(a) and 3(b), respectively. However, for the same porosity, variations in void distribution influence the free surface velocities Δu and Δt_{sp}, ultimately leading to differing layer rupture strengths.

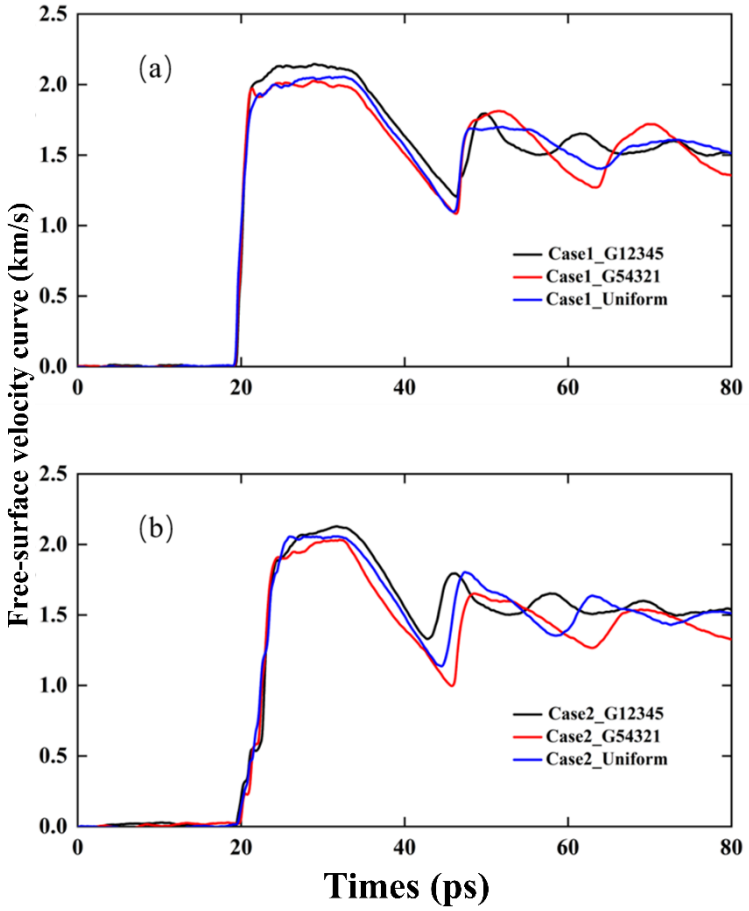


Figure 3. Free surface velocity curves under different void distributions: (a) Case 1 and (b) Case 2 at v = 2.0 km/s

Fig. 3 shows the spalling strength σ_{sp} under simulated conditions in Table 2. Research indicates that under identical loading conditions, the spalling strength σ_{sp} decreases with increasing porosity. This primarily stems from higher porosity generating greater heat during pore collapse under impact compression. Elevated temperatures consequently lead to reduced spalling strength. Furthermore, even at the same porosity level, spalling strength may fluctuate due to variations in pore distribution.

Table 2 Impact and spalling parameters under different void distributions and porosities

Case	v	Porosity	Δu	σ_{sp}
Case1_G12345	2.0km/s	3.73%	0.94463	20.90Gpa
Case1_G54321			0.95443	21.11Gpa
Case1_Uniform			0.96016	21.24Gpa
Case2_G12345	2.0km/s	10.91%	0.86794	19.20Gpa
Case2_G54321			0.86025	19.03Gpa
Case2_Uniform			0.87382	19.33Gpa

3.3. Mechanism of Pore Collapse

Fig. 4 illustrates the dislocation nucleation and distribution in the V2 void within Case2_Uniform. For descriptive convenience, as shown in Fig. 4(a), the large circle perpendicular to the impact loading direction is defined as the "equator," while other circles parallel to the void surface and the 'equator' are defined as "latitude circles." The latitude angle of a latitude circle is defined as its radius, and the angle between this radius and the horizontal line is denoted as α. The reflection angle of the shock wave is denoted as θ.

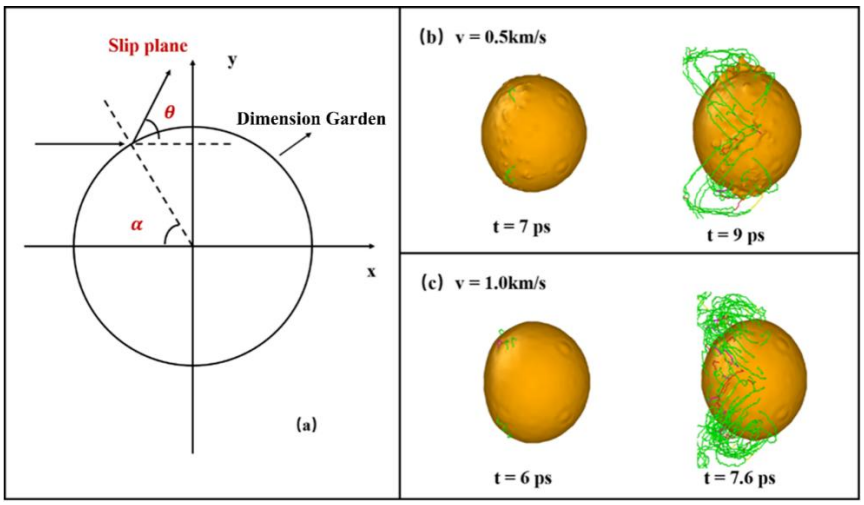


Figure 4. (a) Schematic of plane wave reflection at a void surface. (b) Dislocation snapshots in the V2 void of the Case2_Uniform sample at v=0.5 km/s and (c) at v=1.0 km/s.

As shown in Fig. 4(b), when the impact velocity v = 0.5 km/s, the corresponding impact intensity is insufficient to cause complete collapse of the void, yet it can induce dislocation nucleation on the void surface. T = 7 ps marks the time when the first dislocation appears on the void surface, with the dislocation distribution covering a dimensional angle α = 50°–55°. At t = 9 ps, as the shock wave sweeps past the void, dislocations form on the void's rear surface, distributed within the angular range α = 125°–130°, as shown in Fig. 4(b). At v = 1.0 km/s, as depicted in Fig. 4(c), the initial dislocation emergence location resembles that at v = 0.5 km/s. At t = 6 ps, dislocations appear on the front surface of the void, existing at a dimension angle of α = 50°–55°. At t = 7.6 ps, the shock wave reaches the rear surface of the V2 void, with dislocations appearing at a dimension angle of α = 125°–130°. Additionally, at an impact velocity of v = 2.0 km/s, the initial dislocation nucleation positions on the cavity surface are similar to those at the two aforementioned velocities. Notably, dislocation nucleation occurs earlier as the impact velocity increases. The results indicate two characteristics in the dislocation distribution within the cavity under different impact intensities. First, the arrival of the shock wave front at the void surface triggers the earliest dislocation nucleation. The earliest dislocation appears at an azimuthal angle of α = 50°–55° on the front void surface and 125°–130° on the back surface. Second, after the shock wave sweeps through the void, the front surface generates more dislocations than the back surface, acting as a dislocation source.

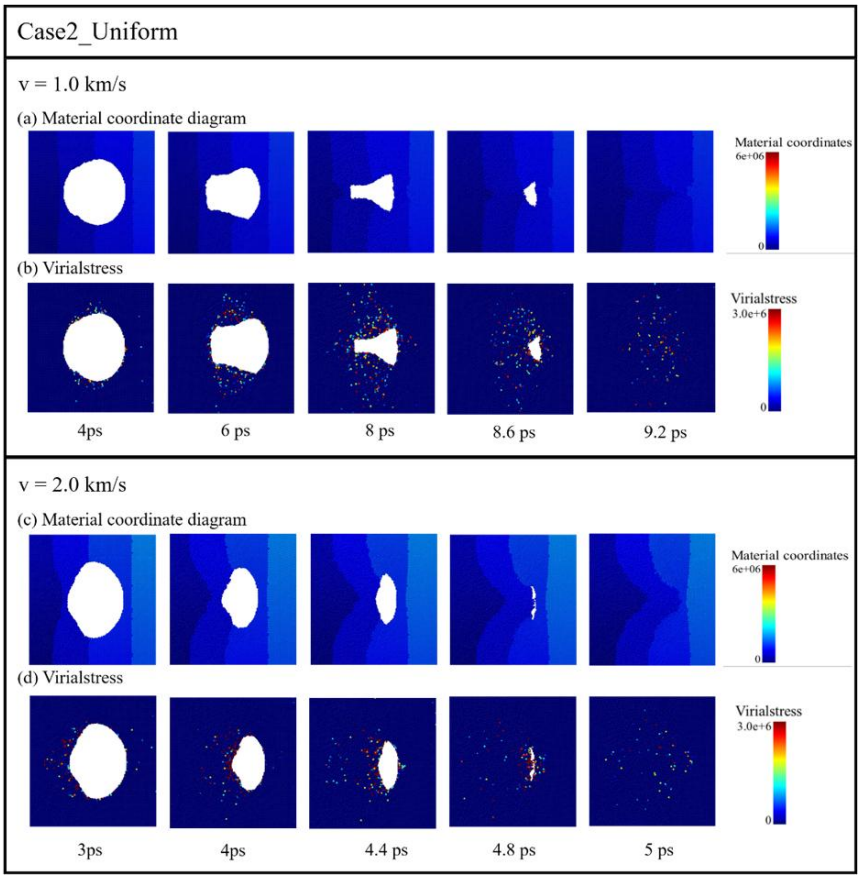


Figure 5. Collapse Process of V1 Void in Case2_Uniform

To elucidate the collapse mechanism of voids, the entire collapse process of the Case2_Uniform V1 cavity was analyzed at velocities v = 1.0 km/s and v = 2.0 km/s. Fig. 5(a) and (c) display atoms labeled with material coordinates, while Fig. 5(b) and (d) represent the magnitude of the virial stress, respectively. At v = 1.0 km/s, as shown in Fig. 5(a), the first plastic deformation occurs at the top and bottom edges of the cavity at t = 4 ps, with collapse proceeding symmetrically along the central axis. However, the collapse shapes of the front and rear surfaces are asymmetric, with the front surface collapsing more extensively than the rear surface. The Virial stress in Fig. 5(b) was selected to analyze the cause of the symmetrical collapse. It was found that stress was primarily concentrated at the upper and lower edges, with the Virial stress on the front surface being greater than that on the rear surface. At t = 8.6 ps, the front surface collapses completely, with only the sub-cavity on the rear surface visible in the figure. At this stage, the primary cause of collapse is the influence of shear stress. The collapse process at V = 1.0 km/s can be simplified to the model[28] shown in Fig. 6. Following the formation of a shear ring at the location of maximum shear stress, the force field near the void undergoes significant changes. Under the combined influence of shear stress and dislocation motion, atoms in region A become more inclined to fill the void. Due to the basal plane being perpendicular to the impact direction, dislocation motion (plastic mechanism) leads to lateral collapse of the void.

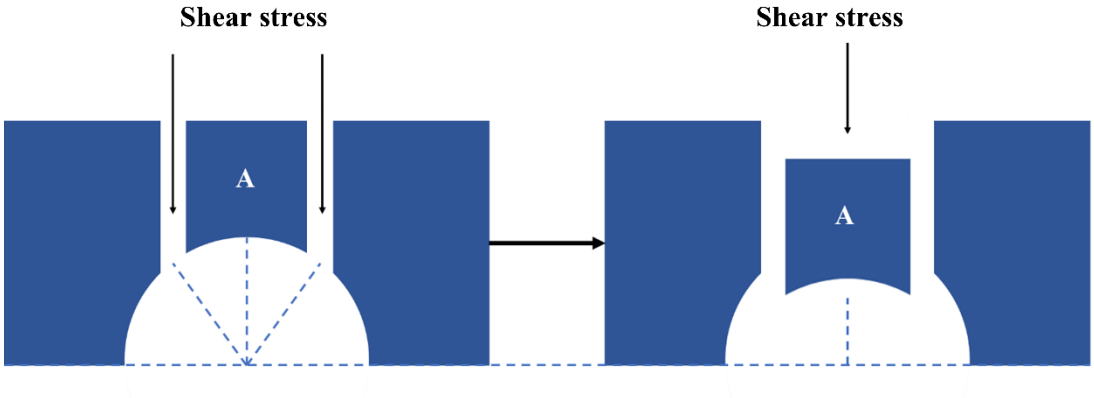


Figure 6. Schematic of the void collapse process at v = 1.0 km/s

When the impact velocity v = 2.0 km/s, the evolution of void collapse is shown in Fig. 5(c), primarily driven by an internal ejection mechanism. Fig. 5(d) reveals that the normal stress is concentrated at the leading edge of the void, indicating a distinct ejection phenomenon. The internal jetting process fills the void longitudinally (along the impact direction), differing from plastic deformation mechanisms. As impact intensity increases, the influence of normal stress becomes more pronounced, allowing shear stress to be neglected. Similar phenomena are also observed in the simulations of Case 1. The fundamental distinction between the plastic deformation mechanism and the internal jetting mechanism in void collapse lies in their dominant stress types: the former is dominated by shear stress, while the latter is dominated by normal stress.

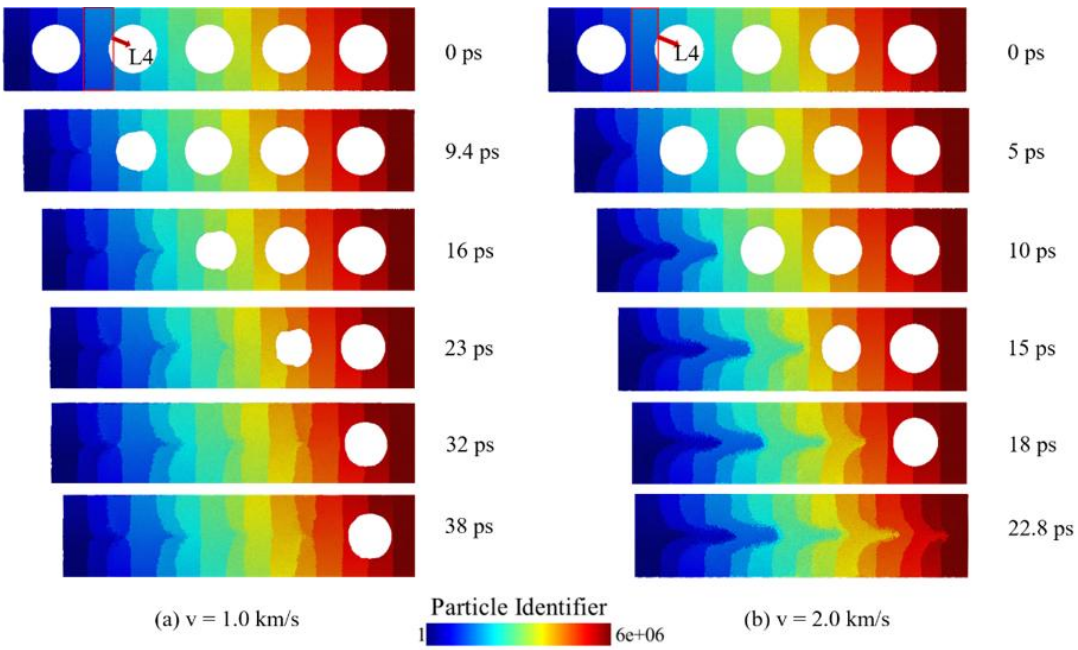


Figure 7. Case2_Uniform Material Coordinate Cloud Diagram at (a) v = 1.0 km/s and (b) v = 2.0 km/s

In addition to the void collapse mechanism, the displacement of atoms between voids during the impact process was investigated. The 6 million atoms in the Case2_Uniform model were divided into 15 slices, labeled L1 to L15 from left to right, as shown in Fig. 7. The results indicate that throughout the entire impact phase, each slice exhibited a compression trend under the influence of the shock wave, with the compression becoming more pronounced at higher velocities. Slice L4 was selected for analyzing atomic displacement between voids. At v = 1.0 km/s and t = 9.4 ps, atoms in L4 first filled the collapse site of the V1 cavity, while the V2 cavity remained intact. At t = 16 ps, the V2 cavity collapsed, and some atoms from the L4 slice filled its collapse site. It is important to note that this process does not affect the filling efficiency of the V1 cavity by the L4 layer. Throughout the subsequent impact process, the filling efficiency of the V1 cavity by the L4 layer remains unchanged. To compare the effect of velocity on atomic displacement within the sample, we selected the Case2_Uniform material coordinate cloud diagram at v = 2.0 km/s, as shown in Fig. 7(b). At t = 5 ps, the collapse of the V1 void caused atoms in the L4 slice to exhibit a tendency to fill the V1 void. However, by t = 10 ps, this tendency changed due to the strong influence of the impact velocity. That is, at higher impact intensities, all slices between voids filled along the impact direction and maintained this trend at subsequent times.

3.4. Temperature propagation during the impact process

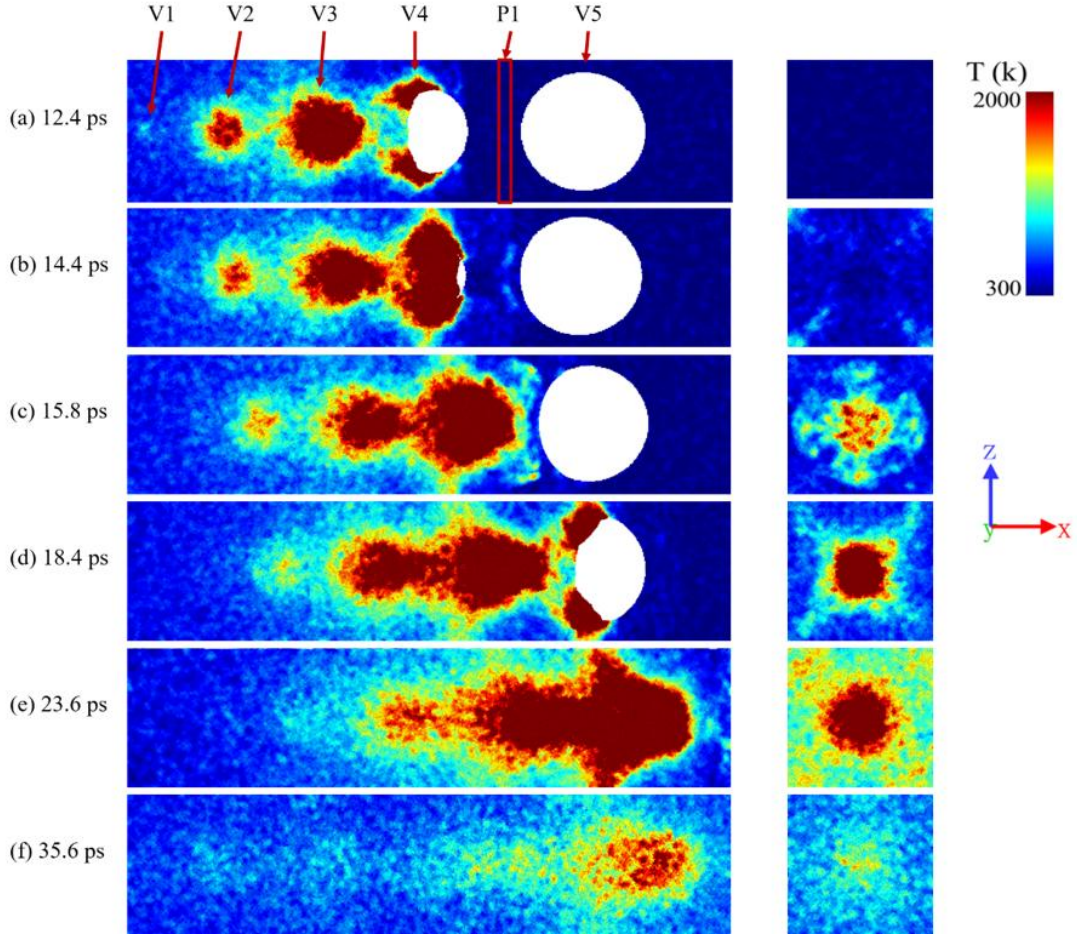


Figure 8. Case2_ G13245 Temperature Evolution Cloud Map, v=2.0 km/s

Porous materials are more prone to forming high-temperature zones than non-porous materials. The formation of these zones is primarily due to additional mechanical work generated by pore collapse and internal jet collisions on pore walls. Fig. 8 illustrates the evolution of the temperature field in the Case2_G12345 model at v = 2.0 km/s. The five voids along the impact direction are designated as V1, V2, V3, V4, and V5. A specific region P1 within the gap-free zone between V4 and V5 was selected for separate analysis. The six contour plots on the right display the left-side view of P1. As shown in Fig. 7, the high-temperature fields generated by all cavity collapses are clearly observable, with varying sizes of these hot spots due to differences in cavity dimensions. Furthermore, temperature evolution is a dynamic process. At t = 12.4 ps (Fig. 8(a)), the temperature field generated by the collapse of void V1 has already diffused, while those from V2-V4 have not fully diffused, appearing as four distinct high-temperature regions in the figure. The evolution of temperature fields from the collapses of other voids follows a similar pattern to that of V1.

Using the P1 slice to analyze the temperature evolution in the void-free region. When the shock wave front reaches the left surface of P1 (Fig. 8(c)), the temperature in the left view of P1 spreads from the center toward the periphery, with a relatively small high-temperature region. At t = 18.4 ps (Fig. 8(d)), the compression wave gradually penetrates the P1 slice,

and the temperature field spreads to all four corners. At t = 23.6 ps (Fig. 8(e)), the compression wave fully penetrates the P1 slice. The high-temperature field in the left view reaches a size comparable to the V4 void, with surrounding temperatures continuing to rise. As shown in Fig. 8(f), temperatures gradually diffuse inward from the high-temperature zone into the sample, with the entire sample now exceeding its initial temperature.

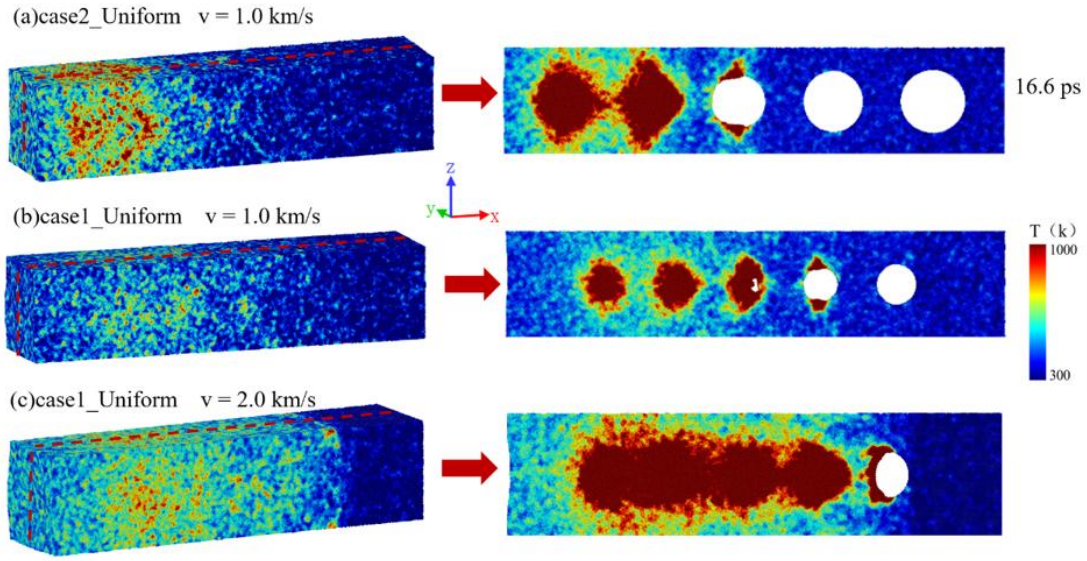


Figure 9. Temperature Contour Map of Uniform Pore Samples at Different Porosities and Velocities

Case2_Uniform (Fig. 9(a)) and Case1_Uniform (Fig. 9(b)) were selected for analyzing the effect of porosity on temperature evolution in the temperature contour plots, with v = 1.0 km/s and t = 16.6 ps. Fig. 9(c) shows the temperature contour plot for Case1_Uniform at v = 2.0 km/s and t = 16.6 ps, used to analyze the impact of shock intensity on temperature evolution. The left panel displays the external temperature contour plot of the sample, while the right panel shows a 10 Å-wide slice selected along the y-axis at the sample center. Comparing the left temperature maps in Fig. 9(a) and Fig. 9(b), the external temperature of Case2_Uniform is higher than that of Case1_Uniform. Firstly, Case2 has a larger porosity than Case1. The free surface area of Case2's pores is greater than that of Case1, leading to more plastic work generated during pore collapse and thus faster temperature rise. Second, the larger pore volume in Case2 places pore surfaces closer to the sample's outer surface. This shortens the thermal conduction path, accelerating heat transfer. Comparing the right-hand side contour plots in Fig. s 9(a) and 9(b), at the same impact velocity, the temperature in Case2_Uniform propagates only to the V3 pore, creating a larger high-temperature zone due to pore collapse. In contrast, the temperature in Case1_Uniform propagates to the V4 pore, causing its collapse, as shown in Fig. 9(b). Therefore, higher porosity results in larger localized high-temperature zones caused by pore collapse and slower temperature propagation within the sample.

Comparing Fig. 9(b) and (c), the impact velocity also affects the size of the high-temperature zone generated by void collapse. When v = 2.0 km/s, as shown in Fig. 9(c), the high-temperature field produced by void collapse is larger, and the high-temperature regions are interconnected. In Fig. 9(b), with v = 1.0 km/s, the lower shock intensity results in only localized high-temperature regions caused by void collapse, with no significant heat transfer observed. Notably, during the initial stages of void collapse, the high-temperature zones coincide with the stress concentration regions. This observation further validates the collapse mechanism described in Section 5.3.4, which arises from the combined effects of forward and transverse flows.

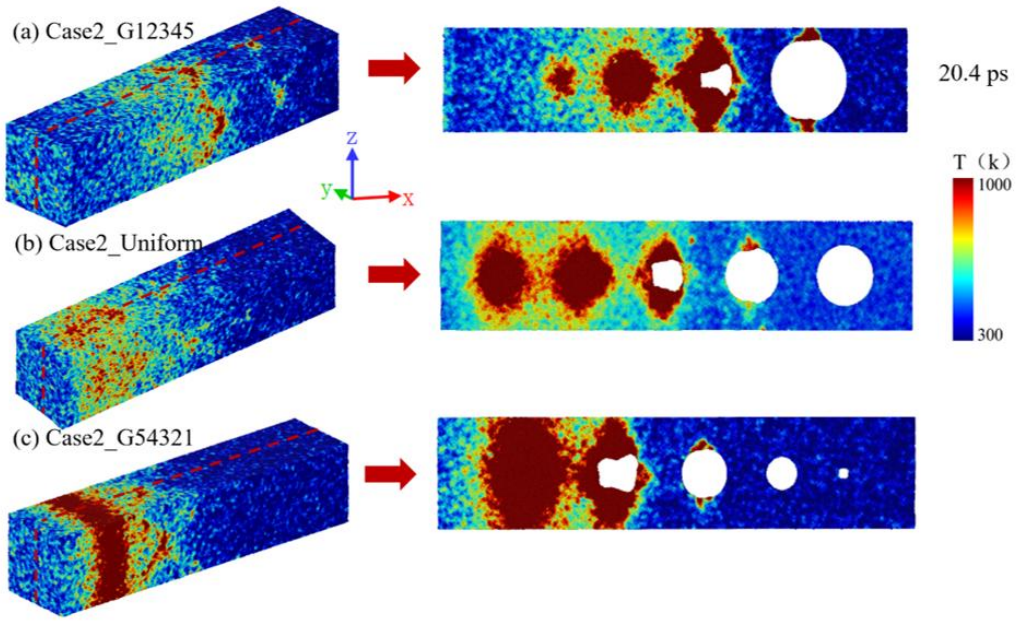


Figure 10. Temperature contour map for Case 2 under different void distributions at v = 1.0 km/s

When v = 1.0 km/s and t = 20.4 ps, Fig. 10 shows the temperature contour plots for Case2 under the G12345, Uniform, and G54321 distributions. The left panel displays the external temperature contour plot of the sample, while the right panel presents a 10 Å-wide slice of the sample along the y-axis. Comparing the arrival positions of wavefronts at t = 20.4 ps: the wavefront of Case2_G12345 reaches the V5 void, Case2_Uniform reaches the V4 void, while the leading edge of Case2_G54321 only reaches the V3 void. This indicates that when void distributions differ, the propagation speed of the compression wave within the sample varies, and consequently, the propagation speed of temperature also differs.

Metal layer cracking impacts virtually every aspect of future production and daily life, making research into damage fracture critically important. As shown in Fig. 11, the temperature contour map and stress-temperature profile of Case2_G12345 at the point of imminent delamination and fracture (v = 2.0 km/s, t = 36.6 ps) were selected to analyze the location of material damage fracture. Fig. 11(a) reveals that the high-temperature field is primarily concentrated in regions with model voids, particularly around voids V4 and V5 where the highest temperatures occur. Comparing this with the temperature-position profile in Fig. 11(c) shows a significant increase in temperature along the impact direction. As delamination fracture is imminent, high stress locations are primarily found in the target's mid-section rather than the highest temperature regions, as shown in Fig. 11(b). This indicates that in porous Ni, when the stress wave reaches the right end face and rebounds toward the sample center, temperature has not fully diffused. Since maximum stress occurs in the model's mid-section, the delamination fracture location should be in this region, where temperature will gradually increase with tensile failure.

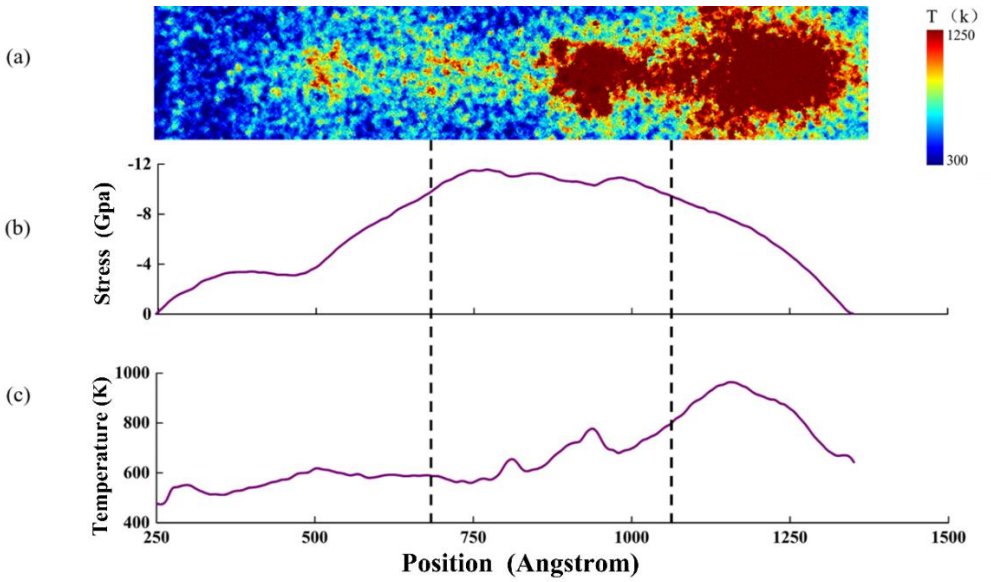


Figure 11. At v = 2.0 km/s and t = 36.6 ps: (a) Damage morphology and thermodynamic distribution for Case2_G12345; (b) Normal stress profile; (c) Temperature distribution.

To validate the above hypothesis, the temperature contour plots, stress distributions, and temperature profiles at v = 2.0 km/s and t = 37.6 ps for Case2_G12345 were selected to analyze the fracture location of the model, as shown in Fig. 12. The location of the spalling fracture precisely corresponds to the region of maximum stress in Fig. 11(b). This occurs because when the impactor, subjected to an instantaneous impact load, is removed from the model, a rarefaction wave is generated at the loading surface. Furthermore, when the shock wave encounters a free surface (here comprising two parts: the free surface behind the target and the free surface of the void), reflection occurs, generating a rarefaction wave propagating in the opposite direction. When these two opposing rarefaction waves meet within the target, significant tensile stresses are generated. The tensile stress along the x-direction exceeds the fatigue strength of Ni, causing cavitation fracture in the target material—specifically, the nucleation, growth, and coalescence of voids—with a gradual increase in temperature.

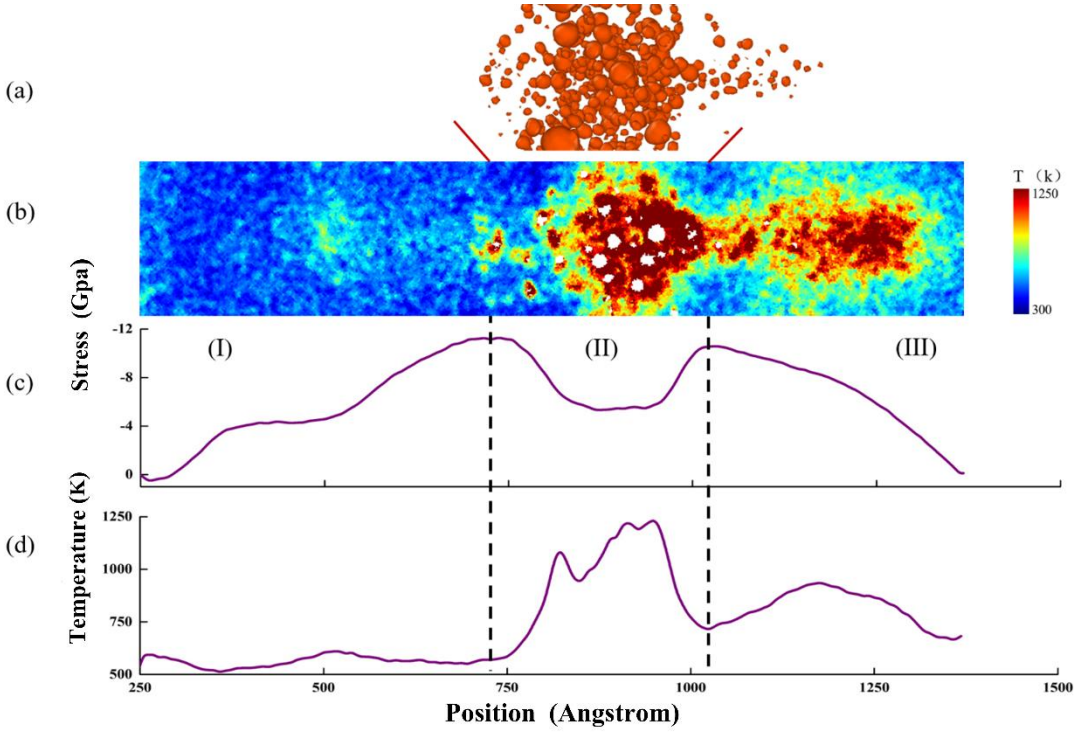


Figure 12. Damage morphology and thermodynamic distribution of Case2_G12345 at v=2.0 km/s and t=37.6 ps. (a) Pore nucleation during layer cracking; (b) Cross-section of damaged sample with atoms colored by atomic temperature; (c) Normal stress profile; (d) Temperature profile.

Based on the fracture location, the sample is divided into three regions along the dashed lines, as shown in Fig. 12: (I) the main region, (II) the cavitation region, and (III) the scattered plate region. Among these, the temperature in region (I) remains stable with no significant fluctuations; region (II), the cavitation zone, exhibits higher temperatures than the other two regions during spalling and fracture. On one hand, most heat is generated due to pore nucleation and growth accompanied by significant tensile stress. On the other hand, as shown in Fig. 12, a high-temperature field accumulates in the scattered plate region prior to delamination fracture, and it cannot be ruled out that temperatures reflected by the thin layer may be carried to the cavitation region. (III) The scattered plate fractures completely, with temperatures higher than those in the main region.

4. Conclusion

This study employs molecular dynamics simulations to investigate the impact response and spalling behavior of porous nickel under varying porosities and pore distributions. The main conclusions are as follows:

(1) In molecular dynamics simulations, when $V/V_0 > 0.7$, the calculated Hugoniot curve for the shock compression response of nanoporous Ni closely matches the experimental results reported by Marsh et al. Molecular dynamics simulations are a viable approach for simulating high-impact loading.

(2) The presence of voids weakens the impact strength of nanoporous Ni, as void distribution influences the propagation path of shock waves within the sample. A higher porosity leads to a more pronounced weakening effect on impact strength. This is primarily due to the differing distributions of rarefaction waves reflected from free surfaces under varying void configurations.

(3) Under identical loading conditions, the spalling strength decreases with increasing porosity. For a given porosity, spalling strength also fluctuates due to variations in void distribution. The reliance on higher porosity leads to greater heat generation during pore collapse under impact compression, further contributing to reduced layer fracture strength. Both pore collapse and layer fracture generate high-temperature zones, with the temperature in the zone produced by layer fracture being significantly higher than that in the zone produced by pore collapse.

(4) Two collapse mechanisms were revealed: the forward

flow mechanism and the lateral flow mechanism. The forward flow mechanism causes the void to neck forward, while the lateral flow mechanism leads to longitudinal vacuum filling of the void. The combined action of forward and lateral flows results in complex collapse evolution. At lower impact intensities, lateral plastic flow dominates over forward plastic flow; at higher impact intensities, both forward and lateral flows interact synergistically. As impact intensity further increases, forward flow becomes dominant, forming an internal jet.

(5) The displacement of atoms between voids changes with impact intensity. At low impact intensity, atoms between two voids primarily fill the collapsed voids on both sides, remaining unchanged in subsequent impact stages. At high impact intensity, atoms between two voids primarily fill the collapsed voids along the impact direction, remaining unchanged in subsequent impact stages.

References

[1] Seitz M W, Skews B W. Effect of compressible foam properties on pressure amplification during shock wave impact[J]. Shock Waves, 2006, 15: 177-197.

[2] Evans A G, Hutchinson J W, Ashby M F. Multifunctionality of cellular metal systems[J]. Progress in materials science, 1998, 43(3): 171-221.

[3] Xiang M, Hu H, Chen J. Spalling and melting in nanocrystalline Pb under shock loading: Molecular dynamics studies[J]. Journal of applied physics, 2013, 113(14): 144312.

[4] Czarnota C, Molinari A, Mercier S. The structure of steady shock waves in porous metals[J]. Journal of the Mechanics and Physics of Solids, 2017, 107: 204-228.

[5] Bonnan S, Hereil P L, Collombet F. Experimental characterization of quasi static and shock wave behavior of porous aluminum[J]. Journal of applied physics, 1998, 83(11): 5741-5749.

[6] Erhart P, Bringa E M, Kumar M, et al. Atomistic mechanism of shock-induced void collapse in nanoporous metals[J]. Physical Review B, 2005, 72(5): 052104.

[7] Krasnikov V S, Mayer A E. Plasticity driven growth of nanovoids and strength of aluminum at high rate tension: Molecular dynamics simulations and continuum modeling[J]. International Journal of Plasticity, 2015, 74: 75-91.

[8] Krasnikov V S, Mayer A E. Plasticity driven growth of nanovoids and strength of aluminum at high rate tension: Molecular dynamics simulations and continuum modeling[J]. International Journal of Plasticity, 2015, 74: 75-91.

[9] Singh M, Singh L P, Husain A. Propagation of nonlinear travelling waves in Darcy-type porous media[J]. Acta Astronautica, 2010, 67(9-10): 1053-1058.

[10] Nield D A, Bejan A. Convection in porous media[M]. New York: springer, 2006.

[11] Madeo A, Gavrilyuk S. Propagation of acoustic waves in porous media and their reflection and transmission at a pure-fluid/porous-medium permeable interface[J]. European Journal of Mechanics-A/Solids, 2010, 29(5): 897-910.

[12] Bruck H A. A one-dimensional model for designing functionally graded materials to manage stress waves[J]. International Journal of solids and Structures, 2000, 37(44): 6383-6395.

[13] Polenov V S, Chigarev A V. Wave propagation in a fluid-saturated inhomogeneous porous medium[J]. Journal of applied mathematics and mechanics, 2010, 74(2): 198-203.

[14] Sun L, Chien C L, Searson P C. Fabrication of nanoporous nickel by electrochemical dealloying[J]. Chemistry of materials, 2004, 16(16): 3125-3129.

[15] Huber N, Viswanath R N, Mameka N, et al. Scaling laws of nanoporous metals under uniaxial compression[J]. Acta 91aterialia, 2014, 67: 252-265.

[16] Pia G, Delogu F. Nanoporous Au: Statistical analysis of morphological features and evaluation of their influence on the elastic deformation behavior by phenomenological modeling[J]. Acta Materialia, 2015, 85: 250-260.

[17] Shu J Y. Scale-dependent deformation of porous single crystals[J]. International Journal of Plasticity, 1998, 14(10-11): 1085-1107.

[18] Ling C, Besson J, Forest S, et al. An elastoviscoplastic model for porous single crystals at finite strains and its assessment based on unit cell simulations[J]. International Journal of Plasticity, 2016, 84: 58-87.

[19] Liu Z G, Wong W H, Guo T F. Void behaviors from low to high triaxialities: Transition from void collapse to void coalescence[J]. International Journal of Plasticity, 2016, 84: 183-202.

[20] Liao Y, Xiang M, Zeng X, et al. Molecular dynamics studies of the roles of microstructure and thermal effects in spallation of aluminum[J]. Mechanics of Materials, 2015, 84: 12-27.

[21] Zhou X W, Johnson R A, Wadley H N G. Misfit-energy-increasing dislocations in vapor-deposited CoFe/NiFe multilayers[J]. Physical Review B, 2004, 69(14): 144113.

[22] Reed E J, Fried L E, Joannopoulos J D. A method for tractable dynamical studies of single and double shock compression[J]. Physical review letters, 2003, 90(23): 235503.

[23] Luo S N, Germann T C, Tonks D L. Spall damage of copper under supported and decaying shock loading[J]. Journal of Applied Physics, 2009, 106(12): 123518.

[24] Marsh S P. LASL shock Hugoniot data[M]. University of California Press, 1980.

[25] Al'Tshuler L V, Bakanova A A, Trunin R F. Shock adiabats and zero isotherms of seven metals at high pressures. 1962.

[26] Isbell W M, Shipman F H, Jones A H. Hugoniot Equation of State Measurements for Eleven Materials to Five Megabars. 1968.

[27] Rice M H, Mcqueen R G, Walsh J M. Compression of Solids by Strong Shock Waves[J]. Solid State Physics, 1958, 6:1-63.

[28] Xiang M, Cui J, Yang Y, et al. Shock responses of nanoporous aluminum by molecular dynamics simulations[J]. International Journal of Plasticity, 2016, 97:24-45.